Studying Atomic Structures by Aberration-Corrected Transmission Electron Microscopy

Knut W. Urban

Seventy-five years after its invention, transmission electron microscopy has taken a great step forward with the introduction of aberration-corrected electron optics. An entirely new generation of instruments enables studies in condensed-matter physics and materials science to be performed at atomic-scale resolution. These new possibilities are meeting the growing demand of nanosciences and nanotechnology for the atomic-scale characterization of materials, nanosynthesized products and devices, and the validation of expected functions. Equipped with electron-energy filters and electron-energy–loss spectrometers, the new instruments allow studies not only of structure but also of elemental composition and chemical bonding. The energy resolution is about 100 milli–electron volts, and the accuracy of spatial measurements has reached a few picometers. However, understanding the results is generally not straightforward and only possible with extensive quantum-mechanical computer calculations.

To see the atomic structure of matter is an old dream in science that has now become a burning issue with the advent of nanoscience and nanotechnology, for which atomic-scale synthesis requires atomic-resolution characterization of the results (1). In the past two decades, substantial progress has been made in electron microscopy (EM) to achieve this objective, and in a limited number of favorable cases, it has been possible to perform structure investigations at atomic-scale resolution (2). However, only the successful construction of aberration-corrected electron lenses in the 1990s (3, 4) set atomic-resolution EM on its path to becoming a more generally applied technique in advanced condensed-matter physics and materials science (5–7).

Over and above the high-precision mapping of atom positions, aberration-corrected EM enables the occupancies of atom sites to be determined and allows atomic-scale imaging of chemical composition and bonding by combining high resolution in energy and space with the use of spatially resolved electron-energy–loss spectroscopy (EELS) to map particular electron states localized at or between atoms. These features explain the large number of orders worldwide for the new generation of aberration-corrected electron microscopes that have come onto the market since around 2004. On the other hand, work with aberration-corrected optics also shows how demanding the new techniques are and that they are as yet by no means routine. Furthermore, because atomic-scale resolution means probing the quantum world, contrary to both intuition

Institute of Solid State Research and Ernst Ruska Center for Microscopy and Spectroscopy with Electrons, Helmholtz Research Center Jülich, D 52425 Jülich, Germany. E-mail: k.urban@fz-juelich.de

and frequently held views, understanding what the "images" show is generally not straightforward. As a consequence, in many cases, the ultimate result of state-of-the-art microscopy is an atomic model on a computer rather than an image.

Scientists employ transmission EM (TEM) in two basically different technical variants (8). In conventional TEM, the specimen is illuminated by a near-parallel bundle of electrons, and the image is formed by a sequence of lenses equivalent, in principle, to those used in a light-optical microscope. In scanning TEM (STEM), a fine probe is formed by optically focusing the incident electrons and is then scanned across the specimen. The transmitted electrons are registered by detectors, and the resulting signal is displayed on a video screen. In conventional TEM, the aberrations of the objective lens are decisive for an image's quality, whereas in STEM, the aberrations of the probe-forming lens determine the quality. In principle, two types of aberrations are always involved: geometrical aberrations, such as spherical aberration, and chromatic aberra-

tions, which arise from the electron-energy dependence of the refraction properties of magnetic fields. Current lens designs can only correct for the former. To reduce the effect of chromatic aberrations, field-emission electron sources and, in some cases, energy filters (monochromators) are used in the electron-beam–forming system of the new generation of 100-to-300-keV instruments.

An ideal converging lens would image a point in the object to a corresponding point in the image. In reality, as a result of aberrations, the image is broadened into a point-spread disk. This is illustrated schematically in Fig. 1A for the case of a spherical aberration. Point spread arises from the refraction power of a real lens increasing with the angle that the beams entering the lens make with its optical axis. As a result, the electrons that scattered in the specimen at high angles come to a focus some distance in front of the Gaussian image plane that is defined by the low-angle beams. The focal length of an electromagnetic lens can be easily varied by adjusting the current through the lens coils. Such defocusing also induces point spread and is treated as an aberration. Although these two represent the most substantial aberrations, there are many more that contribute not only to a broadening but also to an angular distortion of the point-spread disk (6, 9, 10).

Progress has been achieved in recent years because systems that are largely free of aberrations can be constructed with aberration compensation brought about by adding to a lens optical elements that exhibit the same aberrations as
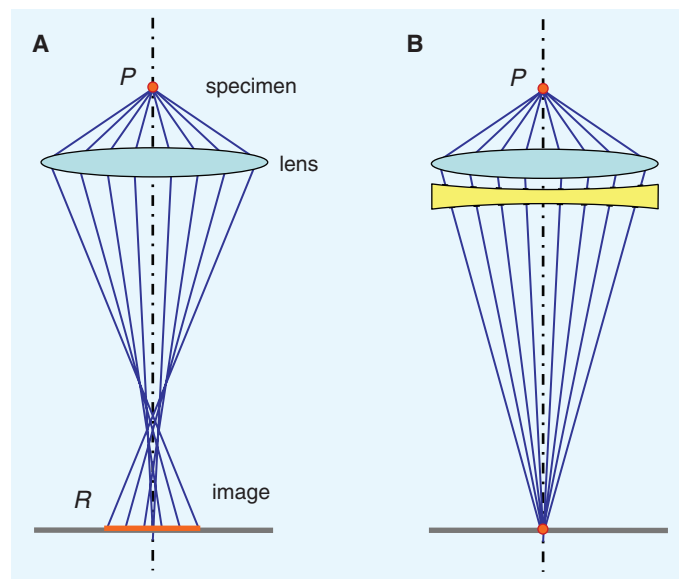

Fig. 1. (**A**) Schematic illustration of spherical aberration of a converging lens. The scattering power increases with the increasing angle (with respect to the optical axis) at which the electrons enter the lens. As a result, the focal length of the beams passing the lens at its periphery come to a focus a distance in front of the Gaussian image plane that is defined by the paraxial, low-angle beams. The image of a point *P* of the specimen is broadened into a "point-spread disc" of radius *R*. (**B**) Spherical aberration is compensated by combining the converging lens with a suitable diverging lens. In electron optics, diverging lenses are realized by combinations of multipole lenses.

the lens but of the opposite sign. In particular, the spherical aberration of a converging lens is corrected by adding a diverging lens that compensates for the too-high refraction power of high-angle scattered beams (Fig. 1B). This is achieved by a double-hexapole system (11, 12) in conventional TEM and in STEM. For the latter, multiple quadrupole-octopole systems (10, 13) are also used.

Conventional TEM

The basis for studying atomic structures by TEM is the quantum mechanical interaction of the incident electron wave field with the atomic potential. It is this interaction that supplies information about the specimen's interior structure. This information is contained in the electron wave function at the exit plane of the specimen. It is this wave function that is representing the object for the subsequent optics. Although individual single atoms deposited on a transparent substrate can be imaged by using TEM, the bulk of the work concerns crystalline structures. Because of the limited resolution of the optical system, these are usually oriented in such a way that a major crystallographic axis is adjusted to be parallel to the direction of the incident electron beam. Thus, the projected lateral atom distances are adopting maximum values, and the atom columns extending along the viewing direction are imaged end-on.

The exit-plane wave function cannot be derived in a straightforward way from the intensity distribution in the image. This is because atomic structures are phase objects; because phases (equivalent to Zernike phase-contrast microscopy in light optics) cannot be "seen," contrast has to be created by deliberately introducing particular phase shifts into the electron wave field by suitably defocusing the objective lens. This is the basis of the classical Scherzer technique of phase-contrast TEM (14). However, the defocus-induced phase shifts are highly nonlinear in angle and affect the image intensity distribution in a very complex manner; thus, there is no direct way to derive the desired exit-plane wave function.

A solution to this problem is provided by computer-based wave-function retrieval techniques. There are a number of variants, but all have in common that the microscope is operated as an interferometer, which exploits the fact that the objective lens introduces phase shifts into the electron waves. The technique most widely used is the focus-variation technique (15, 16). A series of typically 20 images are recorded by a charge-coupled device camera while the objective-lens focus is varied incrementally step by step. These images are transferred, pixel by pixel,

into a computer, where the exit-plane wave function is calculated via least-squares fitting to a simulated image series (17). Besides defocus, all other lens aberrations also affect the image intensity distribution, which requires the handling of typically more than 10 parameters. These values must either be known from dedicated scattering experiments (9) or compensated to negligible values before taking the image series.

In spite of some progress (18, 19), no technique is known that allows us to calculate the potential and the underlying structure "backwards" from the exit-plane wave function. The solution is to do a "forward" calculation, in which a Schrödinger form (with relativistically corrected electron mass and wavelength) of the Dirac equation in small-angle approximation is solved numerically for a model structure based on a first guess and iteratively improved to obtain a best fit between the calculated and experimental exit-plane wave function. In addition to the formidable task of properly adjusting in the model the positions of a large number of atoms with atomic precision, this procedure is hampered by the fact that in atomic dimensions there is no direct access to such important imaging parameters as sample thickness and the precise direction of the incident electrons. There is no other solution but to treat these parameters as variables that have to be determined in the fitting procedure. The result generally is therefore not an image in the conventional sense but a computer model of the structure that gives the atomic species and coordinates. These procedures are facilitated if the structure is known in some areas of the imaged sample region because this information can be used as a reference. This is

the case if defects in otherwise perfect structures are investigated. Also, the presence of various types of atoms with major differences in atomic scattering power accelerates the computer fit. In very thin samples, computer modeling benefits from the projected-potential approximation, according to which the maxima in maps of the phase part of the complex electron exit-plane wave function are considered as a projection of the atomic-potential minima in the sample (8).

The new contrast theory for aberration-corrected instruments shows that optimum contrast at a minimum point spread can be achieved by combining a small defocus with a small negative value of the spherical-aberration parameter C_S, produced by overcompensation by a few percent of the value in the uncorrected instrument (20). Under these negative spherical-aberration imaging (NCSI) conditions, atoms appear bright on a dark background; the contrast is so strong that oxygen and other light atoms, such as nitrogen or even boron, can be seen in the original images (21). This is substantial progress as compared with conventional TEM, in which oxygen could only be seen in the reconstructed exit-plane wave function (15, 22). Besides the reduction in point spread, which is equivalent to higher resolution, the dramatic increase in contrast achieved by NCSI is considered to be one of the major advantages of spherical-aberration correction (23, 24).

An example for NCSI is given in Fig. 2, showing a $\Sigma 3\{111\}$ twin domain boundary in $BaTiO_3$. With reference to the schematic of the structure, all the atom species, including oxygen (arrows), can be identified in the image. By quantitatively evaluating the local intensity signal, the occupancy (the fraction of sites occupied in a given atomic column seen end-on) can be measured. As depicted in the upper part of the figure, the occupancies thus obtained amount to only 40 to 70% of the bulk value far away from the defect (25). This provides direct evidence of oxygen deficiency at the $\Sigma 3\{111\}$ boundaries in $BaTiO_3$. The corresponding change of the electronic states provides an explanation for the detrimental influence of this type of defect on the electronic properties. Such measurements are not possible in uncorrected instruments because the intensity measured at a given atomic site is falsified by the effect of aberration-induced point spread, leading to parasitic or "cross-talk" intensity at this site originating from neighboring atoms.

The described quantitative techniques have also been applied successfully to investigate lattice defects, stacking faults, and dislocation cores in GaAs and InGaAs/GaAs-based
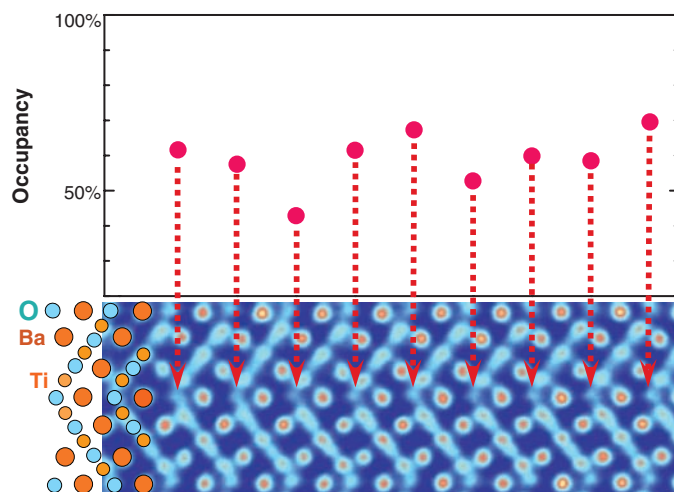

Fig. 2. $\Sigma 3\{111\}$ twin boundary in $BaTiO_3$. All atomic species, including oxygen, can be identified. The atomic resolution is confirmed by image simulations. These indicate that, because of negligible point spread, neighboring atoms have no effect on the intensity measured in a given atomic position. This provides the basis for the quantitative site-occupation measurements. The local intensity values indicate that, in the individual oxygen-atom columns seen end-on, only between about 40 and 70% of the sites are occupied. This provides evidence for oxygen deficiency, which is presumed to have a detrimental influence on electronic properties [adapted from (25)].

heterostructures at atomic resolution (*26*). An investigation into the surfaces of nanometer-sized platinum catalyst particles provided clear evidence that the outermost layers consist of irregular islands of atoms favorable to the dissociation of H_2 and O_2 molecules (fig. S1) (*27*).

Resolution and Accuracy in Conventional TEM

The resolution of an electron microscope is generally specified on the basis of a Rayleigh-type criterion, that is, by the distance at which two atomic contrast maxima can be separated in the image (*8*). For the current generation of aberration-corrected 300-keV instruments, this value is about 80 pm (0.08 nm). The accuracy at which the separation of well-isolated atoms can be measured is, however, better by more than an order of magnitude. In a study of 90°-tilt grain boundaries in $YBa_2Cu_3O_7$ (fig. S2), atom relaxations as small as 6 pm were measured, and an accuracy below 5 pm was demonstrated using an aberration-corrected instrument with a Rayleigh resolution of 120 pm (*28*).

This precision of aberration-corrected conventional TEM allows values for physical parameters to be derived directly on the atomic scale. This was demonstrated by an investigation into the structure of polarization domain walls (Fig. 3A) in the ferroelectric Pb$(Zr_{0.2}Ti_{0.8})O_3$ (PZT) (*29*). Ferroelectricity arises from characteristic shifts of atoms on the unit-cell scale, which induce charge-dipole formation by lowering the local symmetry. The picometer-precision measurement of the shifts of individual atoms, including oxygen (Fig. 3B), allowed the derivation, unit cell by unit cell, of the local strength and direction of the polarization vector.

STEM

As in conventional TEM, access to the specimen structure is provided in STEM by the quantum mechanical interaction of the incident electron wave field with the atomic potential. However, there are two major differences that are decisive for image formation in STEM. The first arises from the geometry of the fine probe rastered across the specimen. It is formed as the tip of a cone produced by a convergent bundle of electrons. The asso-

ciated angular range of the incident electrons gives rise to characteristic electron states inside the sample and to a corresponding electron exit-plane wave function. The second characteristic of STEM arises from the detector geometry beneath the specimen. Depending on the radial position of the detector, STEM offers two different imaging modes. Bright-field imaging is based on the low-angle scattered electrons, yielding images subject to phase contrast in a manner similar to that described for conventional TEM. However, the prevailing imaging mode for STEM is high-angle annular dark-field (HAADF). This is based on a ring-shaped detector collecting electrons

scattered by angles between several tens to about one hundred milliradians. In this mode, the interference effects between electron states responsible for the complex contrast behavior in conventional TEM do not show up in the images because their contributions are effectively averaged out over the detector area (*30*, *31*). What remains is an intensity modulation resembling that formed by electron waves moving through the specimen as bound states along laterally independent atomic columns. The corresponding absence of lateral interference effects means that the observed contrast arises from incoherent scattering. The great advantage of this imaging mode is that the incoherent intensity distributions can be understood directly in terms of atomic structure. Because the scattered intensity depends on the nuclear charge number Z, allowing different atomic species to be distinguished, the HAADF mode is therefore also referred to as Z-contrast imaging.

The spatial-intensity profile of the probe is, in a manner equivalent to conventional TEM, related to the point spread induced by the aberrations of the probe-forming optics. Correcting the spherical aberration allows the beam diameter to be reduced; thus, higher resolution is achieved (*32–34*). A study on GaN and AlN quantum well structures demonstrated that both resolution and contrast determine the eventual result. In this study, the direction of the electric polarization field resulting from locally uncompensated electronic charges could be derived by quantitatively evaluating the asymmetric Al-N pair contrast (Fig. 4A). In spite of the low probe diameter of about 0.07 nm, the 0.011-nm-wide Al-N pairs could not be resolved as two well-separated maxima because the high-Z aluminum dominated the contrast, partly obscuring the low-Z nitrogen (*35*). In a study of a silicon crystal along a crystallographic [112] direction, the atom-pair separation of 78 pm was clearly resolved (Fig. 4B) (*36*). The direct interpretability of the HAADF images in terms of atomic structure enabled the discovery of a new type of reconstruction of the $NiS_2/Si(001)$ interface (*37*). In another study of platinum trimers on alumina surfaces, high-resolution measurements in aberration-corrected HAADF allowed single atoms to be imaged
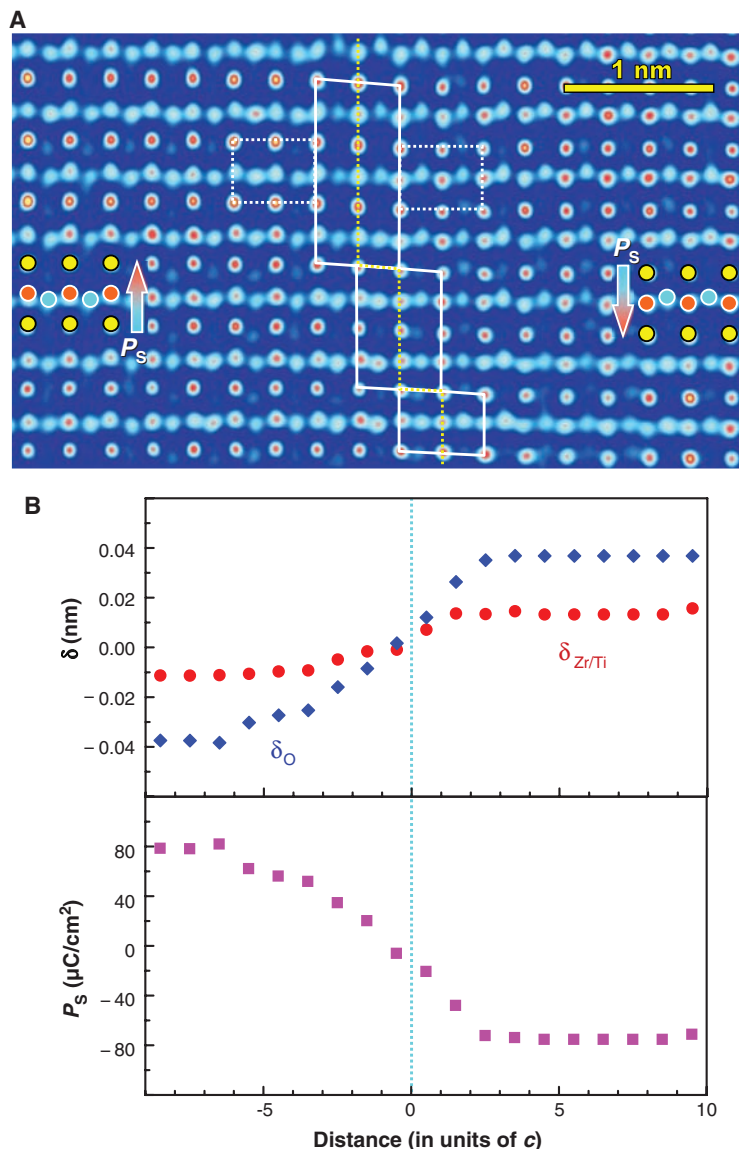

Fig. 3. (**A**) Transversal inversion polarization-domain wall in ferroelectric PZT. Arrows give the direction of the spontaneous polarization, which can be directly inferred from the local atom displacements. The shifts of the oxygen atoms (blue circles) out of the Ti/Zr-atom rows (red circles) can be seen directly, as well as the change of the Ti/Zr-to-Pb (yellow circles) separation. (**B**) Atomic resolution measurements of the shifts of oxygen (δ_O), and titanium/zirconium ($\delta_{Ti/Zr}$) atoms in a longitudinal-inversion domain wall and the value of the local polarization P that can be calculated from these data [adapted from (*29*)].
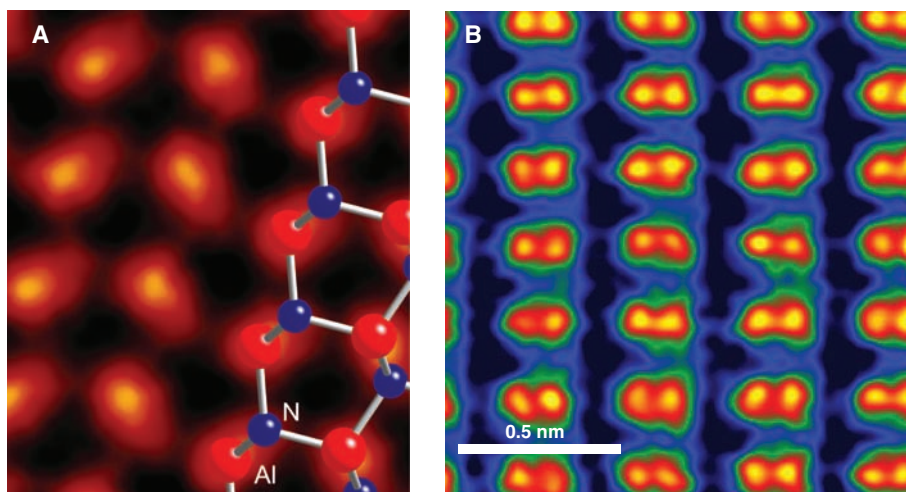
Fig. 4. HAADF images in STEM. (**A**) AlN in [−2,1,1,0] projection. Although the close Al-N pairs, 0.11 nm apart, cannot be resolved as separated entities in the 120-keV instrument, the contrast allows, as confirmed by quantum mechanical calculations, the identification of the bright maximum as Al whereas the tail belongs to N (see ball-and-stick model). This asymmetry can be used to determine the local lattice polarity [from (35)]. (**B**) Si along a crystallographic [112] direction. The atom-pair separation of 78 pm is clearly resolved in the 300-keV instrument [adapted from (36)].
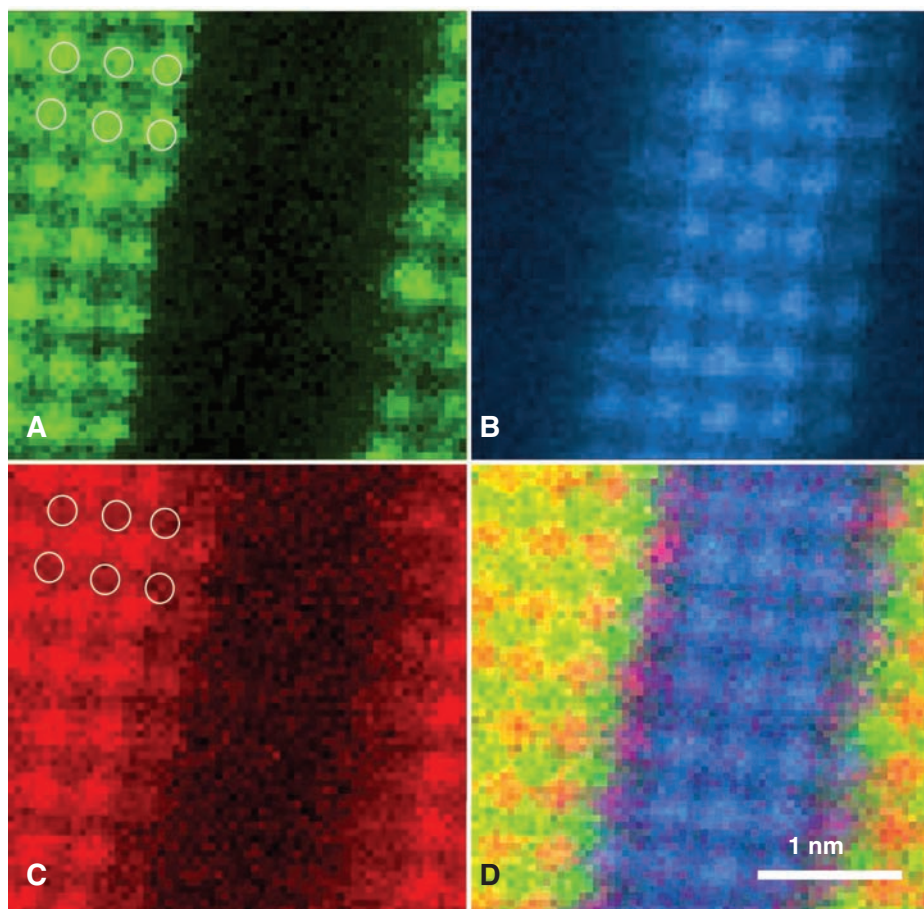

Fig. 5. Spectroscopic imaging of a $La_{0.7}Sr_{0.3}MnO_3/SrTiO_3$ multilayer showing the different chemical sublattices in a 64-×-64-pixel spectrum image extracted from 650-eV-wide EELS data recorded at each pixel. (**A**) La-M edge. (**B**) Ti-L edge. (**C**) Mn-L edge. (**D**) Red-green-blue false-color image obtained by combining the rescaled Mn, La, and Ti images. The purple color at the interface in (D) indicates Mn-Ti intermixing at the Ti sublattice. White circles indicate La atom columns [adapted from (41)].

and different chemical compounds to be differentiated (fig. S3) (38).

The annular detector used for HAADF allows the low-angle scattered electrons to pass. These electrons can be used for EELS, using a spectrometer placed beneath the detector plane. This configuration permits an atomic-scale–resolution analysis of the electronic structure by line traces or by two-dimensional mapping (39, 40). Spherical-aberration correction enables the aperture angle of the probe to be opened up, thus increasing the beam current by several orders of magnitude, which is particularly advantageous for chemical mapping (41). Because the scattering cross sections for inner-shell ionization processes are relatively low, dwell times (for the acquisition of one pixel of data) for obtaining adequate counting statistics are comparable to the time scale on which specimen drift and other instabilities manifest themselves. In a recent-generation aberration-corrected instrument, the total acquisition time was only 30 s for an atomic-resolution 64-×-64-pixel 450–eV-wide high–signal-to-noise EELS spectrum image of $La_{0.7}Sr_{0.3}MnO_3/SrTiO_3$ multilayers (Fig. 5) (41). This demonstrated an increase in signal intensity and a corresponding reduction in dwell time by about two orders of magnitude as compared with uncorrected instruments (42). The high quality of these data allow chemical bonding states to be explored on an atomic scale.

With probe sizes becoming smaller, the spatial resolution becoming higher, and EEL investigations becoming more quantitative, higher-order effects neglected in earlier treatments have to be considered. First of all, this concerns the depth dependence of the quantum mechanical localization of the probe's electron wave field in the sample potential. Interpretation of spectrum images is further complicated by the nonlocal nature of the core-loss electron-interaction potential (43, 44). As a result, the local intensity distribution in a spectrum image may deviate considerably from the geometry of the atomic sites responsible for a specific energy loss. This makes the interpretation of results of studies of bonding variations and modifications of the electronic density of states at defects and interfaces more difficult. Therefore, theoretical modeling, similar to that in quantitative conventional TEM, is now considered an essential part of quantitative high-resolution EELS mapping.

The Future

Developments in electron optics are continuing to improve the resolution even further, beyond that of the present generation of aberration-corrected instruments. These efforts are, above all, driven by an increasing demand for instrumentation, allowing high-precision measurements to characterize the structural, physical, and chemical properties of synthetic nanometer-scale structures, such as clusters, organic and inorganic fullerenes, carbon nanotubes, epitactic heterostructures with particular layer and interphase properties, and interface engineering, to produce materials with

new synthetic electronic properties. A very active field that is benefiting substantially from modern EM techniques is oxide electronics (*45*, *46*), which has recently been highlighted by the discovery of superconductivity in the interface of the two insulating perovskites $LaAlO_3$ and $SrTiO_3$ (*47*). In all these nanostructures, local atom displacements on the picometer scale and subtle changes in the electron bonding configuration occur at interfaces over distances of atomic dimensions. These generally are outside the range of even the most sophisticated x-ray–scattering techniques used for structure investigations. In addition, subtle changes in electronic structure and bonding occur on the atomic scale. As compared with TEM, synchrotron-radiation experiments offer higher energy resolution, but their spatial resolution is lower by several orders of magnitude.

A resolution of 50 pm was recently claimed in factory tests of an instrument developed within the U.S. Department of Energy's Transmission Electron Aberration-corrected Microscope (TEAM) project. The TEAM instrument offers both TEM and STEM operation and employs an improved spherical-aberration corrector technology together with a monochromator in the electron-beam forming system. In a second stage of development, an additional corrector for chromatic aberrations (*48*) will be implemented. The availability of chromatic in addition to spherical correction will not only further improve the image quality, it will also allow the construction of large-gap pole-piece lenses. These will provide sufficient space around the specimen position for the accommodation of micromanipulation devices, allowing in situ dynamic studies under direct observation. Examples are structural transformations during heating or cooling or chemical reactions in a controlled gas atmosphere. Another field of development concerns the improvement of spectral electron-energy resolution. Although commercial energy-loss spectrometers offer a resolution of typically 100 meV, a resolution of 55 meV has recently been claimed in the German Sub-Electronvolt Sub-Ångström Microscope (SESAM) project. This improved resolution can be exploited to study small changes in the width of the local electron-energy band-gap near interfaces in multilayer semiconductor nanodevices (*49*).

In most cases, atomic-resolution TEM is used to obtain a two-dimensional projection of the specimen structure averaged along the electron propagation direction. Although not entirely excluded, elucidating structural and chemical variations along the depth coordinate turns out to be quite difficult in practice. In fact, the scattering effects induced by single atoms are dif-

ficult to trace back to a particular depth position in the sample by using quantum mechanical calculations. Three-dimensional electron tomography attempts to overcome this limitation (*50*). In a recent study on octahedral MoS_2 fullerenes, it was shown that the NCSI technique has the potential for enabling tomography with three-dimensional atomic resolution (*51*). Another technique for obtaining information in three dimensions is based on the fact that the large probe aperture angles in STEM achieved by aberration-corrected optics result in a substantially reduced depth of focus; in principle, this allows depth-sectioning of samples (similar to confocal light microscopy) (*52*). This technique has been successfully used to image single Hf atoms at a depth resolution of about 1 nm in amorphous SiO_2 (*53*).

A recent study in which gold nanoparticles were imaged at atomic resolution by electron holography indicates that this technique benefits from a remarkably increased signal-to-noise ratio when carried out with an aberration-corrected instrument (*54*). On the other hand, electron holography offers the potential to measure, in addition to the structure, local electrical polarization fields on the atomic scale—for example, in nitride-heterostructures or in ferroelectric domain boundaries.

The ultimate quantum mechanical limit to resolution is set by the width of the electron wave function inside the specimen. Because of Heisenberg's uncertainty principle, the extension of the wave function is always larger than the width of the scattering potential, which makes the limit a function of nuclear charge (*55*, *56*). For silicon ($Z = 14$), the width of the wave function of 300-keV electrons is about 70 pm. This is close to what is observed with present-day optics. Therefore, it mainly will be the heavier elements that are expected to benefit from further progress.

References

1. S. J. L. Billinge, I. Levin, *Science* **316**, 561 (2007).
2. D. J. Smith, *Rep. Prog. Phys.* **60**, 1513 (1997).
3. M. Haider, H. Rose, S. Uhlemann, B. Kabius, K. Urban, *Nature* **392**, 768 (1998).
4. N. Dellby, O. L. Krivanek, P. D. Nellist, P. E. Batson, A. R. Lupini, *J. Electron Microsc. (Tokyo)* **50**, 177 (2001).
5. M. Varela et al., *Annu. Rev. Mater. Res.* **35**, 539 (2005).
6. M. Lentzen, *Microsc. Microanal.* **12**, 191 (2006).
7. D. J. Smith, *Microsc. Microanal.* **14**, 2 (2008).
8. D. B. Williams, C. B. Carter, *Transmission Electron Microscopy* (Plenum Press, New York, 1996).
9. S. Uhlemann, M. Haider, *Ultramicroscopy* **72**, 109 (1998).
10. O. Krivanek, N. Dellby, A. L. Lupini, *Ultramicroscopy* **78**, 1 (1999).
11. H. Rose, *Optik* **85**, 19 (1990).
12. M. Haider et al., *Ultramicroscopy* **108**, 167 (2008).
13. O. L. Krivanek et al., *Ultramicroscopy* **108**, 179 (2008).
14. O. Scherzer, *J. Appl. Phys.* **20**, 20 (1949).
15. W. M. J. Coene, G. Janssen, M. Op de Beeck, D. Van Dyck, *Phys. Rev. Lett.* **69**, 3743 (1992).
16. W. M. J. Coene, A. Thust, M. Op de Beeck, D. Van Dyck, *Ultramicroscopy* **64**, 109 (1996).
17. A. Thust, TrueImage, software (FEI Company, Eindhoven, Netherlands, 2006).
18. M. Lentzen, K. Urban, *Acta Crystallogr. A* **56**, 235 (2000).
19. C. Y. Tang, J. H. Chen, H. W. Zandbergen, F. H. Li, *Ultramicroscopy* **106**, 539 (2006).
20. M. Lentzen, *Ultramicroscopy* **99**, 211 (2004).
21. C. L. Jia, M. Lentzen, K. Urban, *Science* **299**, 870 (2003).
22. C. L. Jia, A. Thust, *Phys. Rev. Lett.* **82**, 5052 (1999).
23. J. C. H. Spence, *Science* **299**, 839 (2003).
24. J. M. Thomas, W. Zou, *ChemPhysChem* **4**, 927 (2003).
25. C. L. Jia, K. Urban, *Science* **303**, 2001 (2004).
26. K. Tillmann, A. Thust, K. Urban, *Microsc. Microanal.* **10**, 185 (2004).
27. L. C. Gontard et al., *Angew. Chem. Int. Ed.* **46**, 3683 (2007).
28. L. Houben, A. Thust, K. Urban, *Ultramicroscopy* **106**, 200 (2006).
29. C. L. Jia et al., *Nat. Mater.* **7**, 57 (2008).
30. P. D. Nellist, S. J. Pennycook, *Ultramicroscopy* **78**, 111 (1999).
31. L. J. Allen, S. D. Findlay, M. P. Oxley, C. J. Rossouw, *Ultramicroscopy* **96**, 47 (2003).
32. P. E. Batson, N. Dellby, O. L. Krivaneck, *Nature* **418**, 617 (2002).
33. P. E. Batson, *Ultramicroscopy* **96**, 239 (2003).
34. G. B. Winkelman et al., *Appl. Phys. Lett.* **87**, 061911 (2005).
35. K. A. Mkhoyan, P. E. Batson, J. Cha, W. J. Schaff, J. Silcox, *Science* **312**, 1354 (2006).
36. P. D. Nellist et al., *Science* **305**, 1741 (2004).
37. U. Falke, A. Bleloch, M. Falke, *Phys. Rev. Lett.* **92**, 116103 (2004).
38. K. Sohlberg, S. Rashkeev, A. Y. Borisevich, S. J. Pennycook, S. T. Pantelides, *ChemPhysChem* **5**, 1893 (2004).
39. M. Varela et al., *Phys. Rev. Lett.* **92**, 095502 (2004).
40. M. Bosman et al., *Phys. Rev. Lett.* **99**, 086102 (2007).
41. D. A. Muller et al., *Science* **319**, 1073 (2008).
42. K. Kimoto et al., *Nature* **450**, 702 (2007).
43. M. P. Oxley, E. C. Cosgriff, L. J. Allen, *Phys. Rev. Lett.* **94**, 203906 (2005).
44. M. P. Oxley et al., *Phys. Rev. B* **76**, 064303 (2007).
45. J. F. Scott, *Science* **315**, 954 (2007).
46. N. Nakagawa, H. Y. Hwang, D. A. Muller, *Nat. Mater.* **5**, 204 (2006).
47. N. Reyren et al., *Science* **317**, 1196 (2007).
48. M. Haider et al., *Ultramicroscopy* **108**, 167 (2008).
49. C. T. Koch et al., *Microsc. Microanal.* **12**, 506 (2006).
50. P. A. Midgley, M. Weyland, *Ultramicroscopy* **96**, 413 (2003).
51. M. Bar Sadan et al., *Nano Lett.* **8**, 891 (2008).
52. A. Y. Borisevich, A. R. Lupini, S. Travaglini, S. J. Pennycook, *J. Electron Microsc.* **55**, 7 (2006).
53. K. van Benthem, *Appl. Phys. Lett.* **87**, 034104 (2005).
54. D. Geiger, H. Lichte, M. Linck, M. Lehmann, *Microsc. Microanal.* **14**, 68 (2008).
55. M. Lentzen, K. Urban, *Microsc. Microanal.* **12** (suppl. 2), 1456 (2006).
56. M. A. O'Keefe, *Ultramicroscopy* **108**, 196 (2008).